Contents lists available at ScienceDirect

Transactions of Nonferrous Metals Society of China

36(2026) 522−537

www.tnmsc.cn

Effect of trace impurity elements on high-temperature corrosion resistance of DD98M alloy

Geng-yi DONG [a], Yijiala YILITI [b], Run-ze YU [b], Jie MENG [c], Wen-jun HAN [b], Kai CHANG [b], Qi-fei ZHANG [a], Xiao-gang YOU [a,*], Yi-nong WANG [b]

[a] Zhongyuan Critical Metals Laboratory, Zhengzhou University, Zhengzhou 450001, China;
[b] School of Materials Science and Engineering, Dalian University of Technology, Dalian 116024, China;
[c] Shi-changxu Innovation Center for Advanced Materials, Institute of Metal Research, Chinese Academy of Sciences, Shenyang 110016, China

Abstract: The influence of varying levels of impurity elements on the hot corrosion resistance of the DD98M alloy in Na_2SO_4+NaCl salt at 950 °C was investigated. The results indicate that the corrosion resistance of the DD98M alloy significantly decreases with an increase in impurity content, and the presence of nitrogen leads to an increase in alloy porosity. These porosities promote the rapid diffusion of molten salt and oxygen into the alloy, resulting in a bilateral diffusion of oxygen and sulfur, which leads to an accumulation of these elements at the oxide−matrix interface. This process contributes to the formation and propagation of interfacial cracks. A growth model was developed for hot corrosion products in alloys with varying impurity elements.

Keywords: molten salts; DD98M alloy; hot corrosion; impurity element

1 Introduction

Single-crystal (SX) superalloys are widely used in the manufacturing of aeroengines and gas turbine blade materials due to their exceptional mechanical properties at high temperatures, resistance to oxidation and hot corrosion, as well as good stability under high temperatures [1−4]. However, alkali metal impurities in the fuel and sulphates (mainly sodium sulphate) formed by the oxidation and combustion of sulphur can adhere to the leaves, leading to hot corrosion at high temperatures and causing unpredictable degradation of materials. This poses significant challenges in predicting the lifespan and maintenance schedules of these components, which can ultimately lead to catastrophic failure of components [5,6]. Consequently, the investigation into the hot corrosion behavior of superalloys remains a significant and pressing area of research, particularly in terms of enhancing the durability and reliability of modern turbine blade materials.

The hot corrosion of superalloys can be classified into two types. Type-I occurs at temperatures ranging from 900 to 1000 °C, whereas type-II occurs within the temperature range of 600−750 °C [7,8]. Type-I hot corrosion occurs through a reaction between the protective oxide layer on the alloy surface and molten sodium sulfate (Na_2SO_4), which melts at 884 °C [7]. In type-II hot corrosion, sodium sulfate (Na_2SO_4) reacts with nickel sulfate ($NiSO_4$) and cobalt sulfate ($CoSO_4$) to form a eutectic phase (with a melting point of 550 °C), which accelerates the surface degradation [8,9]. In contrast to type-I, the initiation of type-II

Corresponding author: *Xiao-gang YOU, Tel: +86-371-67736591, E-mail: youxiaogang1990@163.com

https://doi.org/10.1016/S1003-6326(25)66979-2
Received 3 May 2024; accepted 21 February 2025

hot corrosion requires a high partial pressure of sulfur trioxide (SO_3) [10]. Researchers primarily focus on studying the hot corrosion behavior at about 900 °C and the oxidation behavior at approximately 1000 °C [11]. As the inlet temperature of industrial gas turbines (IGTs) continues to rise, the blade surface temperature exceeds 1000 °C, necessitating a more in-depth investigation into the hot corrosion behavior of superalloys at temperatures above 950 °C.

Currently, the enhancement of hot corrosion resistance in superalloys primarily depends on the strategic regulation of alloying elements and the innovation in surface protective coatings. Chromium (Cr) is recognized as the most important element in preventing hot corrosion. Chromium, vital for its ability to form a stable chromium oxide (Cr_2O_3) layer on the alloy surface, acts as a barrier that prevents the interaction between the molten salt and the underlying matrix [12,13]. In addition, Cr can effectively capture sulfur and inhibit the formation of other harmful liquid sulfides [14,15]. Similarly, aluminum significantly enhances hot corrosion resistance by readily forming alumina (Al_2O_3) in oxidizing atmospheres, which effectively reduces the rate of hot corrosion [16,17]. Ti can effectively absorb sulfur and Cr, and promote the formation of a protective TiO_2 film on the surface of the alloy [7]. The presence of Ta can lead to the formation of solid $NaTaO_3$, which effectively prevents the formation of a molten spinel phase and enhances its resistance against hot corrosion [18]. W and Mo will form acid oxides, which accelerates the corrosion process [19]. The addition of Re can effectively inhibit the diffusion of Ni and Al and increase the stability of Cr_2O_3 and Al_2O_3, and thus plays an important role in protecting the matrix [20,21]. However, in addition to alloying elements, impurity elements such as oxygen (O), nitrogen (N), sulfur (S), and carbon (C) in superalloys also significantly affect the adhesion and integrity of the surface oxide layer [22,23]. Investigations into the effect of impurity elements on the hot corrosion properties of superalloys, however, are very limited. Therefore, it is necessary to thoroughly explore the influence of impurity elements on the hot corrosion behavior and the mechanisms.

This study employs the salt package method to simulate the long-term operational conditions of IGT blades, particularly in scenarios involving sulfate deposition. Hot corrosion tests were conducted on the DD98M alloys with different O, N and S contents. The alloys were exposed to a mixture consisting of 75 wt.% sodium sulfate (Na_2SO_4) and 25 wt.% sodium chloride (NaCl) in order to simulate the corrosive environments. This investigation unravels the impact of impurity elements on the hot corrosion behavior of the DD98M alloy, which provides novel insights into improving the corrosion resistance of superalloys by controlling the impurity elements.

2 Experimental

The master alloy was prepared through vacuum induction melting (VIM) and electron beam smelting (EBS). The single crystal alloy rods with a diameter of 16 mm and a length of 220 mm, were prepared using the crystal selection method in the directional solidification furnace subsequently. Three sets of alloys were named as A1, A2 and A3 in turn based on their impurity content. The contents of oxygen, nitrogen, and sulfur within the alloy were measured using the pulse infrared thermal conductivity O/N/H analyzer (TC-436 AR) and the carbon−sulfur analyzer (CS-3000G), boasting an analytical precision of 0.0001 wt.%. The alloy compositions were analyzed using X-ray fluorescence spectrometry (XRF−1800), and the results are presented in Table 1.

Table 1 Compositions of alloys (wt.%)

Alloy	Ni	Al	Cr	W	Co	Ti
A1	Bal.	5.48	7.28	8.57	8.01	0.80
A2	Bal.	5.42	8.20	8.54	7.98	0.78
A3	Bal.	5.48	8.00	8.54	7.95	0.77

Alloy	Mo	Ta	S	N	O	O+N+S
A1	2.16	5.81	0.0001	0.0004	0.0004	0.0009
A2	2.08	5.68	0.0005	0.0012	0.0010	0.0027
A3	2.04	5.68	0.0008	0.0020	0.0014	0.0042

A standard heat treatment was carried out for the alloys. Firstly, the alloys were held at 1295−1300 °C for 4 h and air cooled to room temperature. A two-step aging was performed subsequently, namely holding at 1080 °C for 8 h and air cooled, and then kept at 870 °C for 24 h before air cooled to room temperature. The alloys were then machined into samples with size of *d*16 mm × 5 mm ([001] orientation perpendicular to the *d*16 mm plane). The microstructures of the DD98M superalloy after heat treatment are shown in Fig. 1. After undergoing standard heat treatment, the eutectic microstructure is effectively eliminated, and the size of the γ' phase is also controlled at a similar level. The top, bottom, and lateral faces of the cylindrical specimens were polished to a 3000-grit in order to standardize the surface condition and minimize the impact of surface roughness. The surface contaminants were removed by conducting three rounds of ultrasonic cleaning in anhydrous ethanol, each lasting for 10 min.

The mass of the DD98M samples was measured using an analytical balance with an accuracy of 0.1 mg. The samples were heated to 300 °C in a muffle furnace, and a mixed solution of 25%NaCl+75%Na_2SO_4 was sprayed onto all sides of the samples. The quality of the deposited salt was controlled to be (1.0±0.1) mg/cm^2. The samples were placed on a quartz crucible, ensuring that the surfaces of the samples were fully exposed to air. The hot corrosion experiments were conducted in an OTF−1200X tube furnace. The experimental temperature was set at 950 °C, and the heating and cooling processes were controlled within 1.5 h. The corundum crucible containing Na_2SO_4 was put into the furnace at the same time. The samples were weighed using an electronic balance before and after heating. After the samples were removed from the furnace, they were rinsed with distilled water, dried by air blowing, and then weighed before being recoated with salt. Each datum represents the mean value derived from three independent samples.

The hot corrosion products on the surfaces were identified by X-ray diffractometer (XRD−6000), with diffraction angles ranging from 20° to 60°. The scanning step size and speed were 0.02° and 2.00° per minute, respectively. The surface morphologies of the corroded samples were observed using laser confocal microscopy (OLS5100). Scanning electron microscope (JSM−7900F) was used to observe the surface and cross-sectional morphologies of the samples after hot corrosion. The element distribution and phase composition of the corrosion products were detected and analyzed using the SEM−EDS and TEM−EDX. The micropores of the DD98M alloy were analyzed using the Xradia 610 Versa XRT equipment, which operated at 190 kV with a three-dimensional spatial resolution of 500 nm.

3 Results

3.1 Hot corrosion kinetics of alloys

The kinetics for hot corrosion of the alloys at 950 °C is illustrated in Fig. 2, which showcases the mass change per unit surface area following hot corrosion. The three alloys have experienced significant degradation, with the A1 alloy exhibiting a mass loss of 84 mg/cm^2 and the A2 alloy of 132 mg/cm^2. The A3 alloy exhibits a more pronounced deterioration compared to the A1 and A2 alloys, resulting in a mass loss of 158 mg/cm^2.

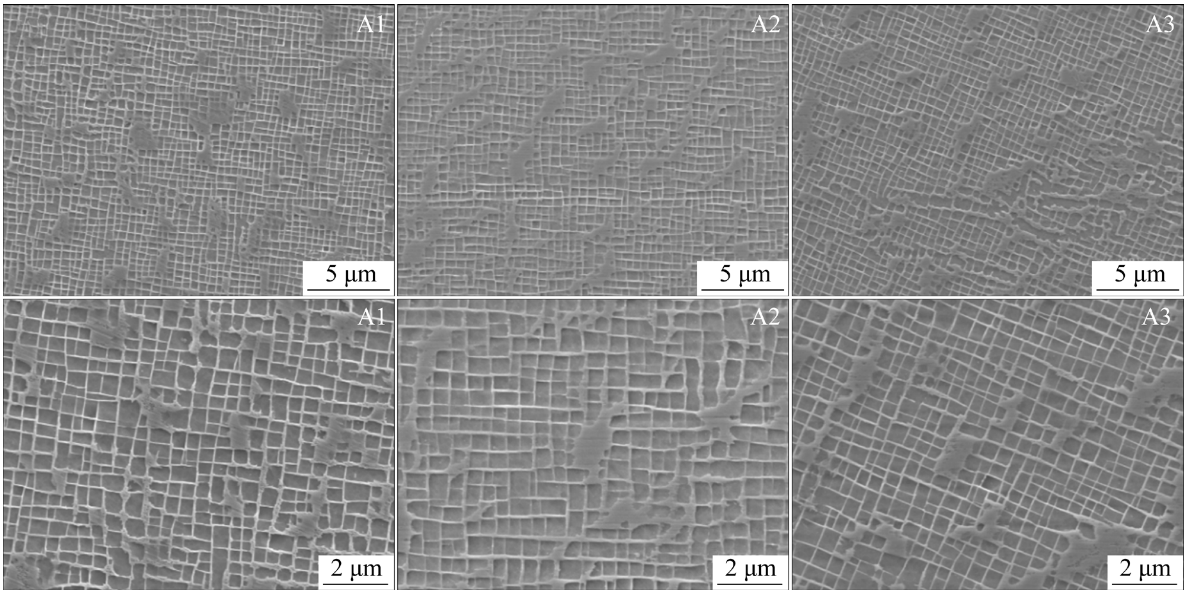

Fig. 1 SEM images of alloys after standard heat treatment

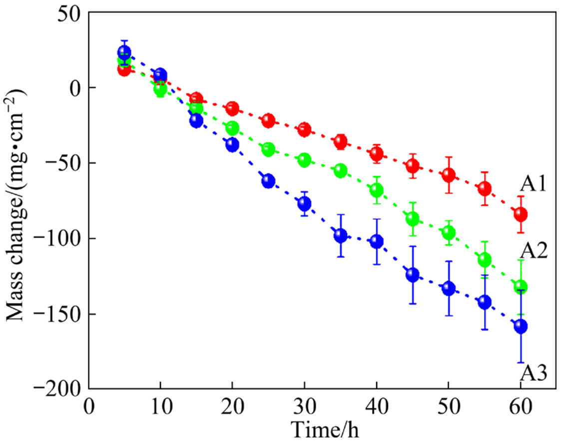

Fig. 2 Mass change versus time curves for alloys during hot corrosion at 950 °C

3.2 Macroscopic morphologies and constituent phase of surfaces

The surface profiles of the DD98M alloys with different impurity contents after 5, 15 and 60 h of hot corrosion are shown in Fig. 3. After undergoing 5 h of hot corrosion in air (Figs. 3(a−c)), the samples exhibit very small surface fluctuations with only a few pits, while maintaining their overall surface integrity. After being exposed to hot corrosion in air for 15 h (Figs. 3(d−f)), the surface profile of the samples shows an increased fluctuation, accompanied by a higher number of pits. Additionally, a small amount of flaking material was observed in the crucible, indicating intensified corrosion. After undergoing 60 h of hot corrosion in air (Figs. 3(g−i)), the surface profile of the samples exhibits significant fluctuations, and a substantial amount of flaking material was observed in the crucible. The severe erosion on the sample surfaces indicates that the integrity of the sample surface can be destroyed by the salt (Na_2SO_4+NaCl). On the whole, the samples with low impurity content exhibit superior surface integrity and smaller profile fluctuations compared to those with high impurity content, indicating enhanced resistance to hot corrosion.

The XRD patterns and compositions of the samples corroded at 950 °C for different durations are presented in Fig. 4. After hot corrosion for 5 h in air, it is observed that complex spinel phases, including $NaTaO_3$, $NiCr_2O_4$, and $NiWO_3$, along with oxides such as Al_2O_3 and NiO, are formed on the surface of the alloys. After 15 h of hot corrosion in air, diffraction peaks of TiO_2 and Cr_2O_3 are observed, as shown in Fig. 4(b). Moreover, the intensity of diffraction peaks for the complex spinel phases ($NaTaO_3$, $NiCr_2O_4$ and $NiWO_3$) is significantly enhanced, indicating their continued growth during hot corrosion. The diffraction peak intensity of $NaTaO_3$ and the matrix gradually weakens after 60 h of hot corrosion in air, as shown in Fig. 4(c). This weakening can be attributed to an increase in the thickness of the corrosion layer. The consistent XRD patterns observed after 15 h of hot corrosion suggest that the corrosion products of alloy remain largely unchanged beyond this duration, indicating that a

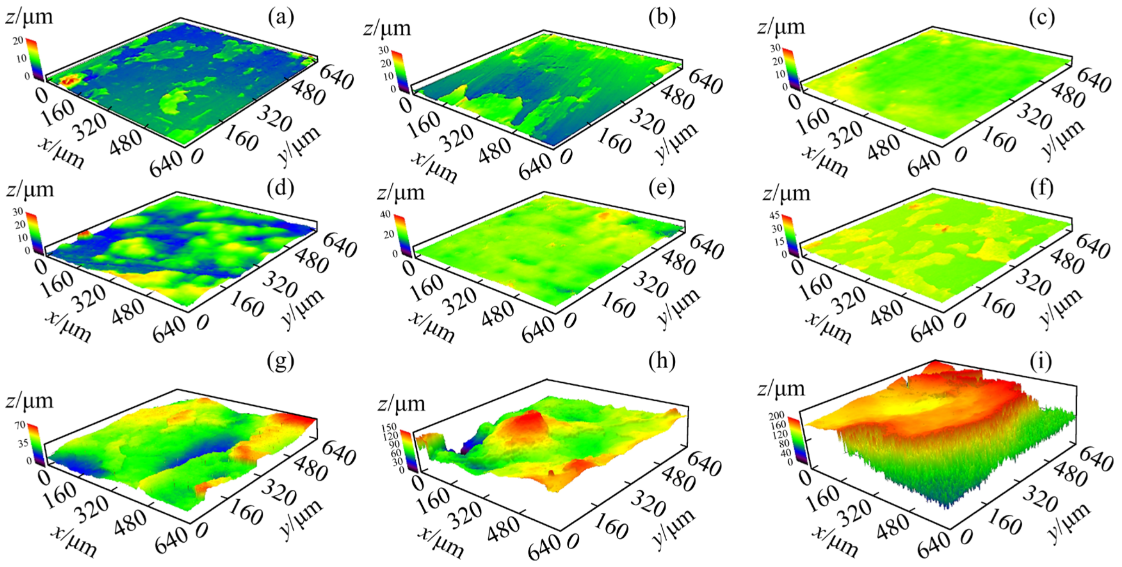

Fig. 3 Macroscopic surface profiles of A1 (a, d, g), A2 (b, e, h) and A3 (c, f, i) alloys after hot corrosion in air for different time: (a−c) 5 h; (d−f) 15 h; (g−i) 60 h

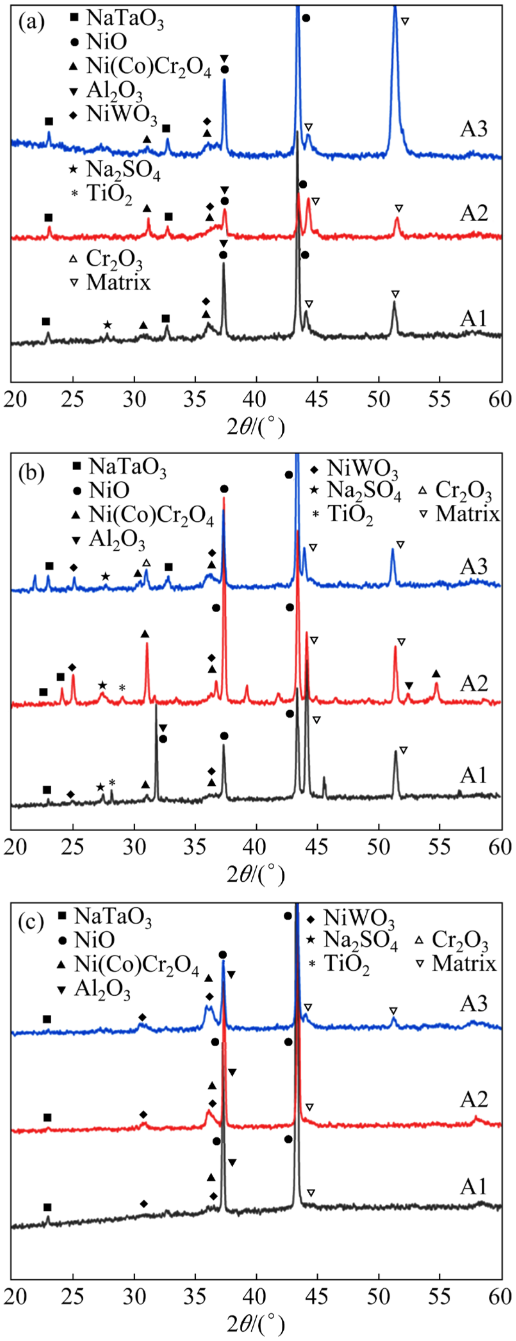

Fig. 4 XRD patterns of samples hot corroded at 950 °C for different time: (a) 5 h; (b) 15 h; (c) 60 h

thickening stage of the corrosion product film has been reached and no new reactions have occurred.

3.3 Surface and cross-sectional microstructures

To elucidate the influence of corrosion layer structure on alloy properties, the surface morphologies in areas without peeling are characterized. The A1 alloy has been chosen as a representative for detailed morphological analysis due to the similar surface morphologies observed in the alloys after hot corrosion at 950 °C for varying durations. A significant amount of oxide particles can be observed on the surface of the A1 alloy after 5 h of hot corrosion in air, as shown in Figs. 5(a−c). These particles are identified as a mixture of NiO and $NiCr_2O_4$ by combining EDS energy spectra with XRD patterns. After hot corrosion for 15 h in air, some small-sized complex oxides are formed in addition to NiO and $NiCr_2O_4$, as depicted in Figs. 5(d−f). The strip-shaped oxides are predominantly identified as chromium, whereas the larger bulk oxides are rich in tantalum. After 60 h of hot corrosion in air, a notable morphological transformation occurs for the NiO and $NiCr_2O_4$ particles on the sample surface. This is characterized by the emergence of numerous protruding structures and an increase in particle size, as depicted in Figs. 5(g−i).

Figure 6 shows the typical surface morphologies of the A3 alloy for different durations of corrosion. After hot corrosion in air, the alloy surfaces peel off seriously in certain regions. Besides, micropores could be observed on the alloy surfaces. Some W-rich acicular oxides are observed surrounding these micropores after hot corrosion for 15 h in air, as shown in Fig. 6(b). Moreover, abnormal protruding structures are observed alongside these micropores, as depicted in Figs. 6(c) and (d). After 60 h of hot corrosion in air, severe shedding is observed around the micropores on the surface of the A3 alloy, as shown in Figs. 6(e, f). The shedding of corrosion products is likely to be influenced by micropores, which can be considered one of the main contributing factors.

The cross-sectional element distributions of the DD98M alloys after being exposed to hot corrosion in air at 950 °C for 5 h are shown in Fig. 7. The cross-section of the alloy after 5 h of hot corrosion reveals a moderate level of hot corrosion. The corrosion products mainly consist of Al oxides with a small amount of Ni and Cr oxides. Besides, sulfides are observed in the oxides, indicating that S has not diffused into the matrix at this stage. The content of Al element is significantly reduced inside the oxides, resulting in the formation of a depleted layer of γ'-phase.

After 60 h of hot corrosion in air (Fig. 8), the thickness of the corrosion layer increases, and a loosely adhered corrosion layer is observed on the

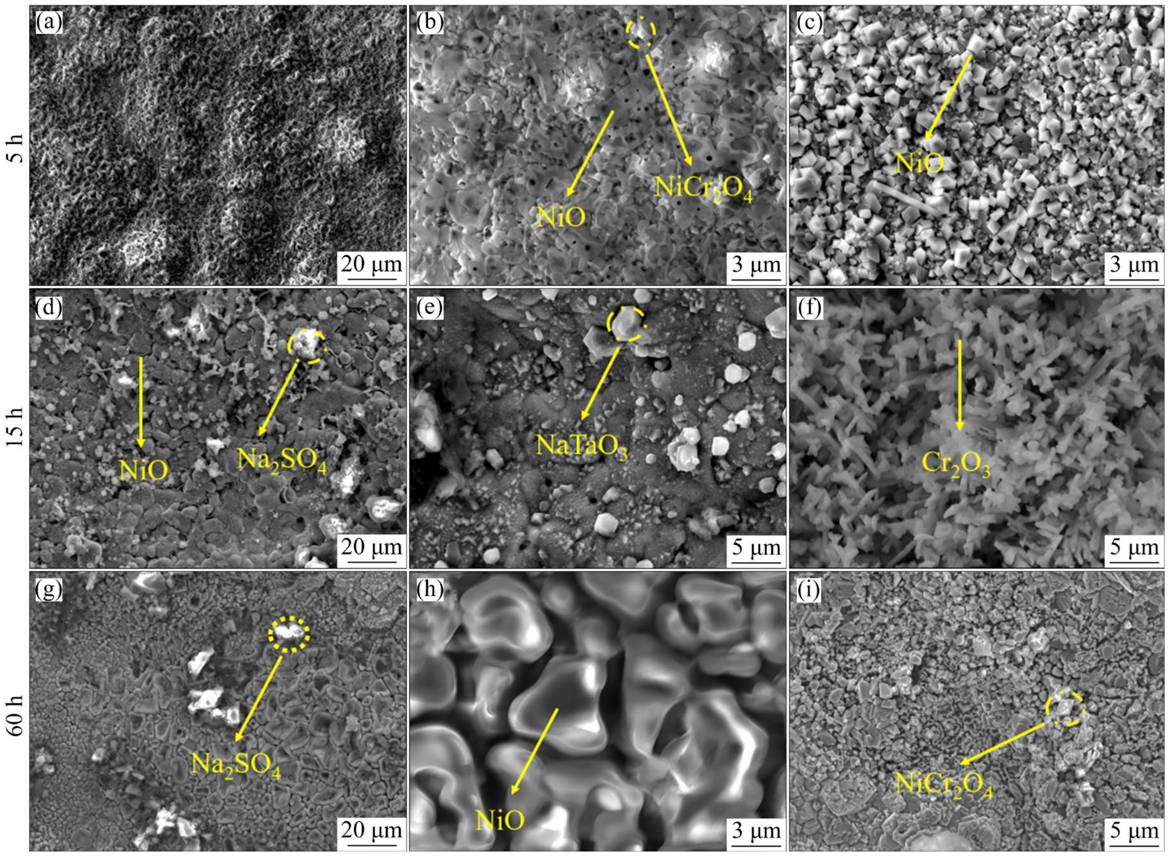

Fig. 5 Morphologies of corrosion products on surfaces of A1 alloy after hot corrosion for different durations: (a−c) 5 h; (d−f) 15 h; (g−i) 60 h

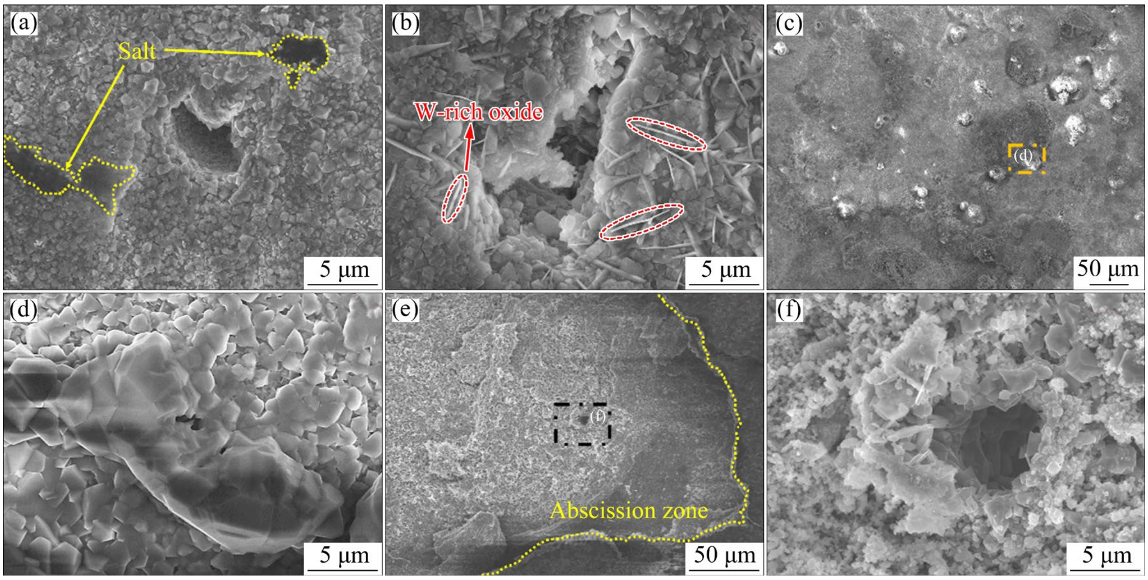

Fig. 6 Morphologies of corrosion products around micropores in A3 alloy after hot corrosion for different durations: (a) 5 h; (b−d) 15 h; (e, f) 60 h

cross-section of the sample. The corrosion products consist of a three-layered structure. The outermost layer is composed of nickel oxide, the middle layer mainly consists of tungsten oxide with small amounts of aluminum and chromium oxides, and the inner layer forms a continuous protective aluminum and chromium oxide layer. The sulphides are also observed in the γ'-phase depleted layer.

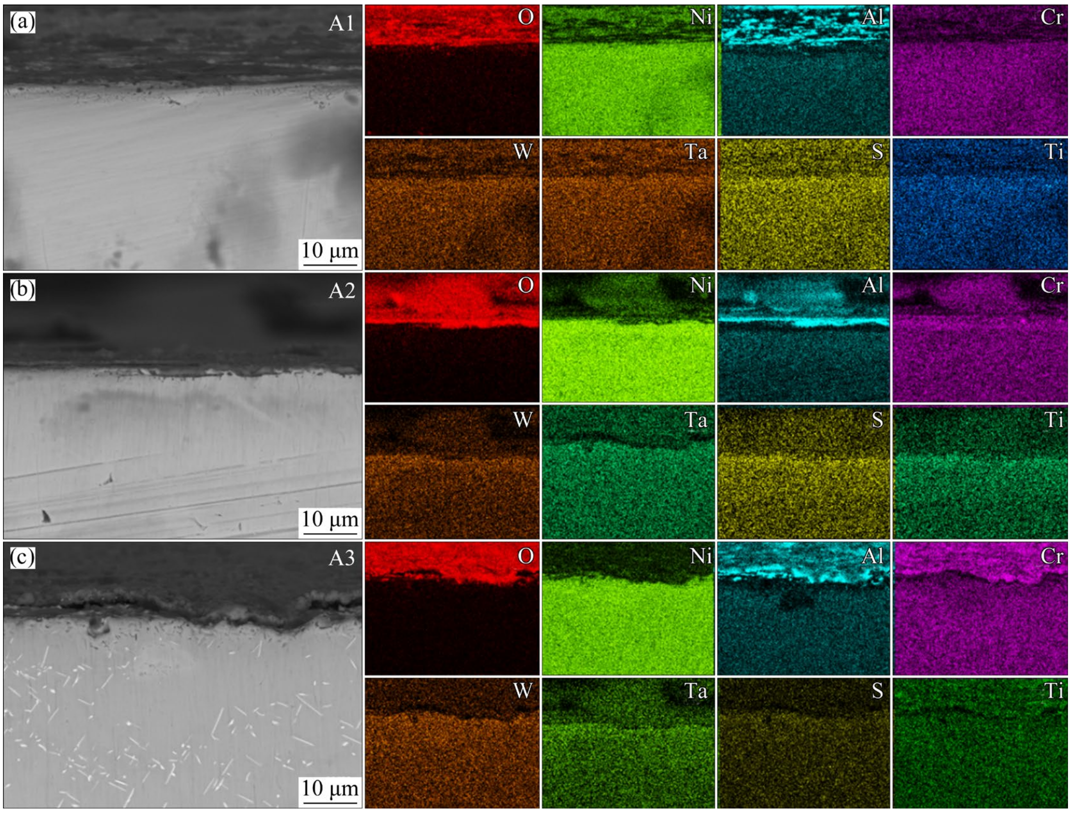

Fig. 7 Distribution of elements on cross section of different alloys after hot corrosion in air at 950 °C for 5 h: (a) A1; (b) A2; (c) A3

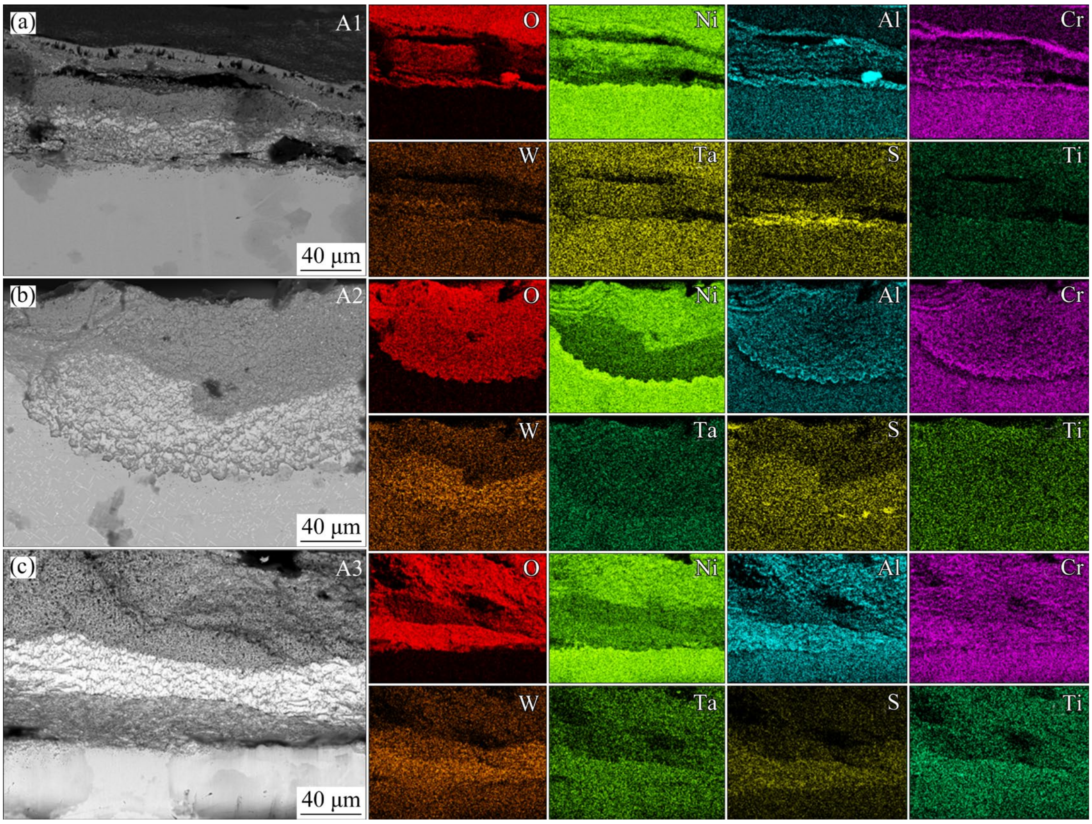

Fig. 8 Distribution of elements on cross section of different alloys after hot corrosion in air at 950 °C for 60 h: (a) A1; (b) A2; (c) A3

To determine the composition of sulfides and the element composition at the interface between the corrosion layer and substrate, focused ion beam (FIB) is used to prepare a cross-sectional specimen of A3 alloy hot corroded in air for 60 h, as shown in Fig. 9. The microstructural analysis, as illustrated in Fig. 9, reveals that a γ' phase depletion region is located between the substrate and the oxide film. Notably, Ta and S exhibit enrichment near the substrate within this depletion region, which is determined as TaS_2 phase based on the fast Fourier transformation (FFT) analysis (Point 4 in Fig. 9). The oxide film adjacent to the substrate is characterized by a high content of Al, Ta, and Cr elements. The diffraction pattern shows that the oxides are Al_2O_3 phase (Point 2 in Fig. 9) and Ta_2O_5 phase (Point 3 in Fig. 9). Its relatively dense structure suggests that it serves as a robust barrier, effectively protecting the substrate from further corrosive damage. The outmost layer, on the other hand, consists of W-rich oxides with numerous micropores distributed throughout its structure. The diffraction pattern indicates that the oxide is $NiWO_4$ phase (Point 1 in Fig. 9). The loose oxide film on the surface is unable to effectively prevent corrosion caused by salt and O_2.

The cross-sectional morphologies and components of A3 alloy after different hot corrosion time are depicted in Fig. 10. After 5 h of hot corrosion in air, residual NaCl salt is observed in the cross-section, along with an oxide layer composed of (Al,Cr)−O. According to the EDS analysis (Table 2), the particles that are black in color are identified as Al_2O_3, and an inconspicuous γ'-phase depleted layer can be observed at the bottom of the oxide layer (Fig. 10(a)). After hot corrosion for 15 h in air, the oxide layer is divided into outer and inner layers. The outer layer primarily consists of NiO, while the inner layer is mainly composed of (W,Cr,Al)−O oxide. It is worth noting that the inner layer contains bright white particles of $NaTaO_3$, which are likely formed through the reaction between Ta-rich oxides and Na_2SO_4 salt. CrS is found in the inconspicuous γ'-phase depleted layer, where S has penetrated through the oxide layer into the γ'-phase depleted layer. After 60 h of hot corrosion in air, the thickness of the corrosion layer increases significantly. This observation suggests that the two oxide layers formed after several hours of corrosion are insufficient in

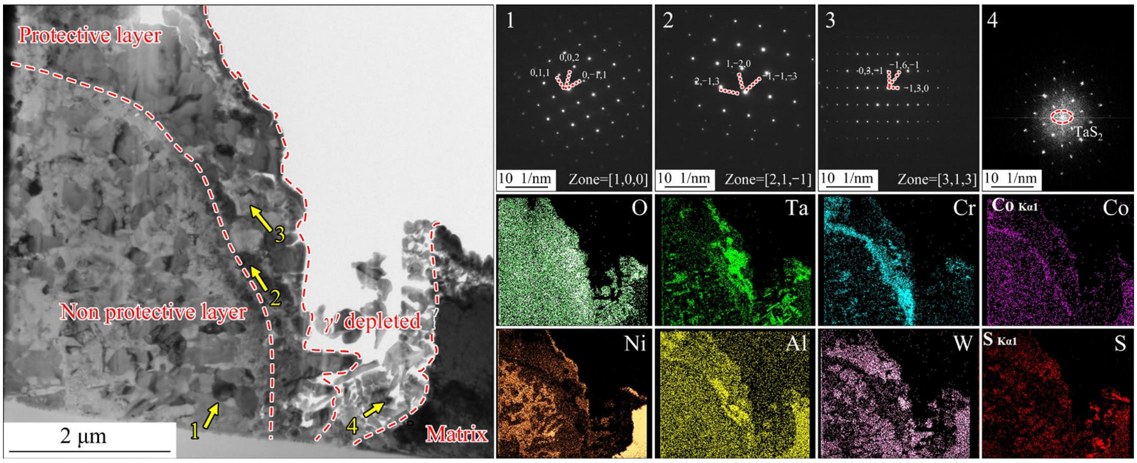

Fig. 9 TEM morphology of interface between corrosion layer and substrate in DD98M alloy

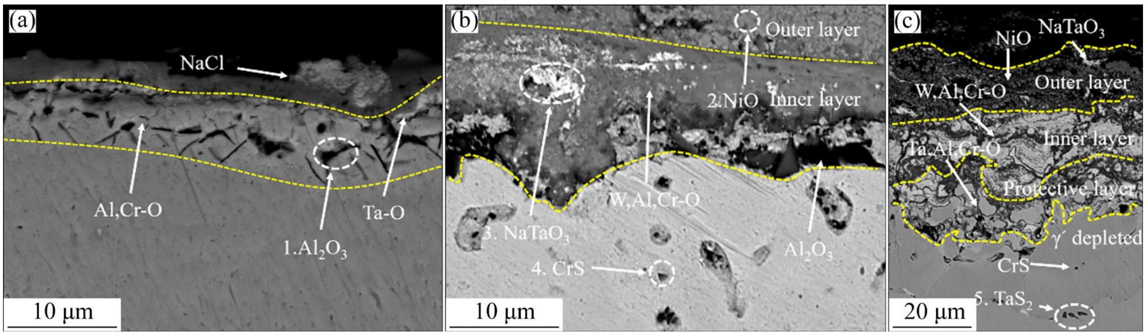

Fig. 10 Morphologies and components of cross-section for A3 alloys after hot corrosion in air for 5 h (a), 15 h (b) and 60 h (c)

preventing further corrosion. The corrosion scale is divided into three distinct layers. The outer layer primarily consists of NiO, with the coexistence of the bright white $NaTaO_3$ phase. The middle layer is a non-protective oxide layer composed of W, Cr, and Al oxides. The innermost layer consists of continuous Ta, Cr, and Al oxides. The γ'-phase depleted layer beneath the innermost protective layer contains CrS and TaS_2. However, TaS_2 is formed at greater depths compared to CrS.

Table 2 EDS results of corrosion products on cross section of A3 alloy (wt.%)

Position in Fig. 10	Ni	Cr	Al	W	Ta	O	S	Na
1	26.6	6.5	30.1	6.1	2.4	27.6	0.3	0.4
2	46	12	4.5	15	4.2	17.8	0.2	0.3
3	23.4	6.1	3.4	5.6	20.6	24.2	0.1	16.6
4	20.2	32.9	0.8	1.4	1.9	2.1	40.5	0.1
5	18.5	1.7	0.7	2.5	25.3	0.8	40.4	0.1

4 Discussion

4.1 Hot corrosion mechanisms of DD98M alloy

The hot corrosion experiments are conducted at temperature higher than the melting point of Na_2SO_4 (884 °C) and NaCl (801 °C). The Na_2SO_4 and NaCl on the alloy surface are in a molten state at the beginning of the experiment. As a result, the following reaction will occur [7]:

$$SO_4^{2-} \rightarrow O^{2-} + S + \frac{3}{2}O_2 \tag{1}$$

During the initial stage of hot corrosion, a limited amount of surface oxygen participates in reactions with the matrix elements. This process is influenced by factors such as the content of alloy elements, their diffusion rates, and the thermal stability of the resulting oxides [12]. Figure 11 shows the standard Gibbs free energy of oxides formed from the oxidation reaction of alloy elements in the DD98M alloy. It can be seen that all elements can spontaneously form oxides with O, and Al, Ti, Cr and Ta are particularly susceptible to oxidation. Due to the low titanium content, the diffraction peaks of TiO_2 can only be observed in the XRD results for alloys after 15 h of hot corrosion in air (Fig. 4(b)). Al_2O_3, Cr_2O_3 and Ta_2O_5 will be preferentially formed on the surface, which is consistent with the observations in Fig. 10(a).

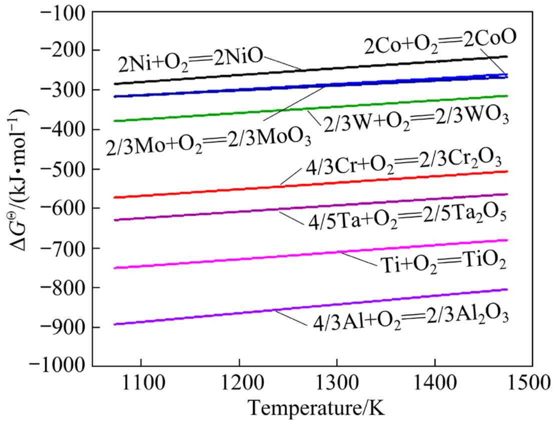

Fig. 11 Standard Gibbs free energy change for oxidation reaction of elements in DD98M alloy

The schematic diagram for the reaction of O_2 with alloy elements during hot corrosion is illustrated in Fig. 12(a). At the same time, Cl^- in the molten NaCl will react with O_2 on the surface and in the air to form Cl_2 (Eq. (2)). With the consumption of O_2, Reaction (1) proceeds more thoroughly and generates more O_2. Additionally, O_2 from the air continuously permeates and reacts with other elements such as Cr and Ni in the matrix. Moreover, Al and Ta diffuse to the surface, which results in the formation of a γ'-phase depletion region inside the matrix. The Cl_2 partially diffuses into the air, while other part permeates through cracks or micropores into the matrix, where it reacts with Al and Cr in the matrix to form volatile compounds such as $AlCl_3$ and $CrCl_3$ (Eqs. (3)−(4)). The volatile chlorides can easily evaporate into the air, leading to a reduction in the Al and Cr content on the alloy surface (Figs. 12(b, c)). The concentrations of Na^+ and O_2^- ions in the molten salt on the alloy surface escalate as Reactions (1) and (2) progress. When the concentration of O_2^- reaches a critical level, dissolution reactions (Eqs. (5)−(7)) occur on the surface oxides.

$$4Cl^- + O_2(g) \rightarrow 2O^{2-} + 2Cl_2(g) \tag{2}$$

$$Al + 1.5Cl_2(g) = AlCl_3,\quad \Delta G(950\ °C) = -527.35\ \text{kJ/mol} \tag{3}$$

$$Cr + 1.5Cl_2(g) = CrCl_3(g),\quad \Delta G(950\ °C) = -319.67\ \text{kJ/mol} \tag{4}$$

$$Na_2O + Ta_2O_5 = 2NaTaO_3,\quad \Delta G(950\ °C) = -147.48\ \text{kJ/mol} \tag{5}$$

$$Na_2O + Al_2O_5 = 2NaAlO_2,\quad \Delta G(950\ °C) = -44.67\ \text{kJ/mol} \tag{6}$$

$$Na_2O + Cr_2O_3 = Na_2Cr_2O_4,\quad \Delta G(950\ °C) = -77.72\ \text{kJ/mol} \tag{7}$$

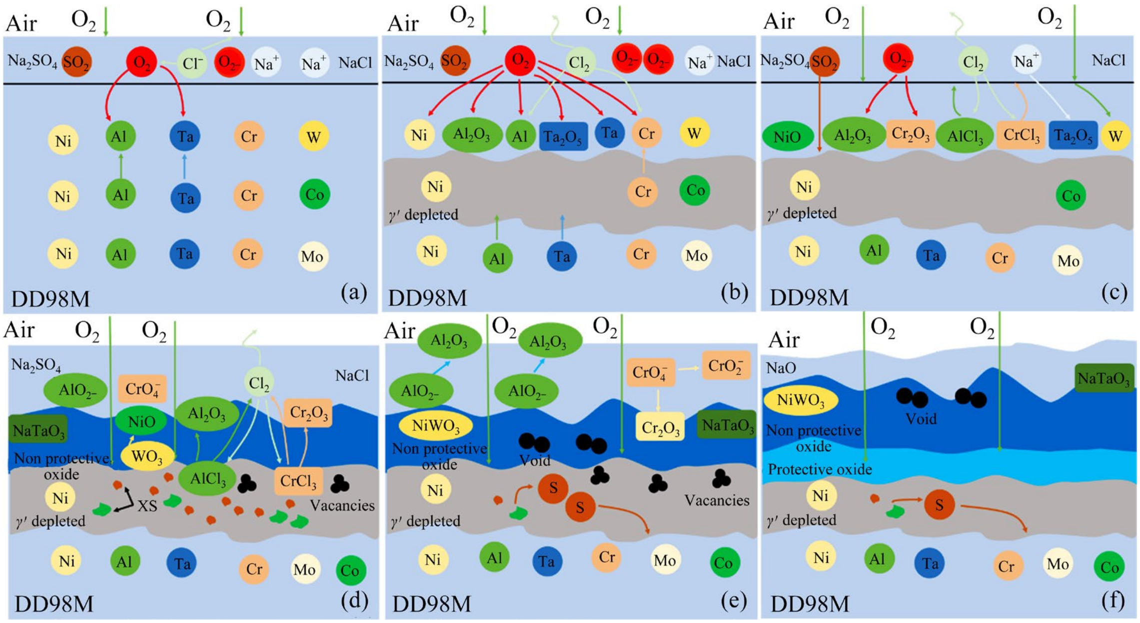

Fig. 12 Schematic diagram for role of Na_2SO_4+NaCl during hot corrosion

The Gibbs free energy of Reactions (5)−(7) indicates a clear preference for the reaction of Na_2O with Ta_2O_5, leading to the formation of a stable $NaTaO_3$ spinel phase, and the schematic diagram is shown in Figs. 12(c, d). The presence of $NaTaO_3$ is confirmed in both the XRD analysis (Fig. 4) and on the cross section of the alloy surface (Fig. 10). Notably, the reaction products of Cr and Al with Na_2O are absent in the XRD analysis shown in Fig. 4. This phenomenon can be attributed to the migration of AlO_2^- and $Cr_2O_4^{2-}$ from the matrix−salt interface to the salt−gas interface. This is coupled with a lower O^{2-} activity at the interface due to the decreased amount of O^{2-} ions resulting from the dissolution of Cr_2O_3 and Al_2O_3, which ultimately leads to a reversal of Reactions (6) and (7). According to the Rapp-Goto model [24], AlO_2^- will reprecipitate at the salt−gas interface to form a non-protective oxide film. Considering that the solubility of Cr_2O_3 is higher at the salt−gas interface than that at the oxide−salt interface, $Cr_2O_4^{2-}$ can dissolve back into the matrix and react with Eq. (8) [24,25], as illustrated in Fig. 12(e). Meanwhile, the volatilized chloride will react with the infiltrated O_2 by Eqs. (9) and (10) to form loose oxides and Cl_2. It can be inferred that Cl_2 functions as a catalyst in the oxidation reaction from Eqs. (3), (4), (9) and (10), thereby expediting the reactions. In addition, micropores are observed on the alloy surface (Fig. 6). The micropores can be considered as diffusion channels for S and O, thereby accelerating the corrosion reaction.

Due to the continuous consumption of oxygen on the surface, the infiltrated oxygen undergoes a reaction with a high content of tungsten to form volatile WO_3. Subsequently, WO_3 diffuses towards the surface and reacts with NiO, resulting in the formation of loosely bounded $NiWO_4$ oxide. Our observations confirm the presence of such oxides, particularly in areas with loose oxide films and micropores on the alloy surface. Moreover, continuous oxidation will increase the partial pressure of S, and loose oxides cannot effectively protect the matrix. As a result, S infiltrates into the matrix and forms sulfides.

$$2CrO_4^{2-}+2SO_2=Cr_2O_3+SO_3+2SO_4^{2-} \tag{8}$$

$$4AlCl_3(g)+3O_2(g)=2Al_2O_3+6Cl_2(g) \tag{9}$$

$$4CrCl_3(g)+3O_2(g)=2Cr_2O_3+6Cl_2(g) \tag{10}$$

The corrosion mechanism of the DD98M alloy in Na_2SO_4+NaCl solution can be summarized, which is also illustrated in Fig. 12. During the initial stage of corrosion, Cl_2 promotes the migration of Cr and Al to the surface, resulting in the formation of loosely bounded oxides. In the meantime, protective Cr and Al oxides are dissolved. The inward infiltration of O_2 and outward diffusion of chloride lead to the consumption of Al and Cr within the matrix. These loose oxides fail to provide effective protection against further infiltration of SO_2 and Cl_2, resulting in the formation of sulfides within the *γ*′-phase depleted layer (Figs. 8 and 10). As the corrosion progresses, the oxidized sulfides release S, which further propagates inward and deepens the corrosion layer. Finally, as the dissolution reaction ceases and Cl_2 continues to volatilize, the higher diffusion rates of Al and Ta compared to other elements facilitate the formation of a protective oxide film on the substrate's exterior, which further impedes diffusion of O and reduces the overall corrosion rate.

The S element infiltrates into the *γ*′-phase depleted layer through the loose metal oxide, as shown in Fig. 10(c). The metal elements will react with S near the *γ*′ phase depleted layer, resulting in their conversion into sulfur compounds and subsequent precipitation. The propensity for sulfide formation is determined by the Gibbs free energy of the reaction and the oxygen partial pressure prevailing at the time of formation, as shown in Fig. 13(a). Therefore, the standard Gibbs free energy of sulfide formation for elements in the DD98M alloy is as follows: $TiS < Al_2S_3 < TaS_2 < CrS < Cr_2S_3 < MoS_2 < WS_2 < CoS < NiS < TaS_3$. According to Fig. 10, only sulfides of Cr and Ta are observed. It is found that TaS_2 is more readily formed than CrS at corrosion temperature of 950 °C. During hot corrosion, oxygen and sulfur penetrate into the matrix and create a content gradient. The formation and distribution of metal sulfides are related to the internal partial pressure of oxygen.

The superposition of the M—O—S stable phase diagram of the DD98M alloy at 950 °C is shown in Fig. 13(b). As depicted in the figure, the order for the critical value of M—O—S oxygen partial pressure is $TiS<Al_2S_3<TaS_2<CrS<XS$ (X=Ni, Co, W, Mo). The formation of sulfides for Ti and Al requires a significantly low oxygen partial pressure. The sulfides of Al and Ti are not observed in the DD98M alloy due to the very small content Ti, and Al preferentially reacts with O. The elements such as Ni, Co, W and Mo require high partial pressure of oxygen to form sulphides. However, their respective sulphides are not observed as they are unable to form stable sulphides under these conditions. Therefore, the formation of sulfides is limited to elements that

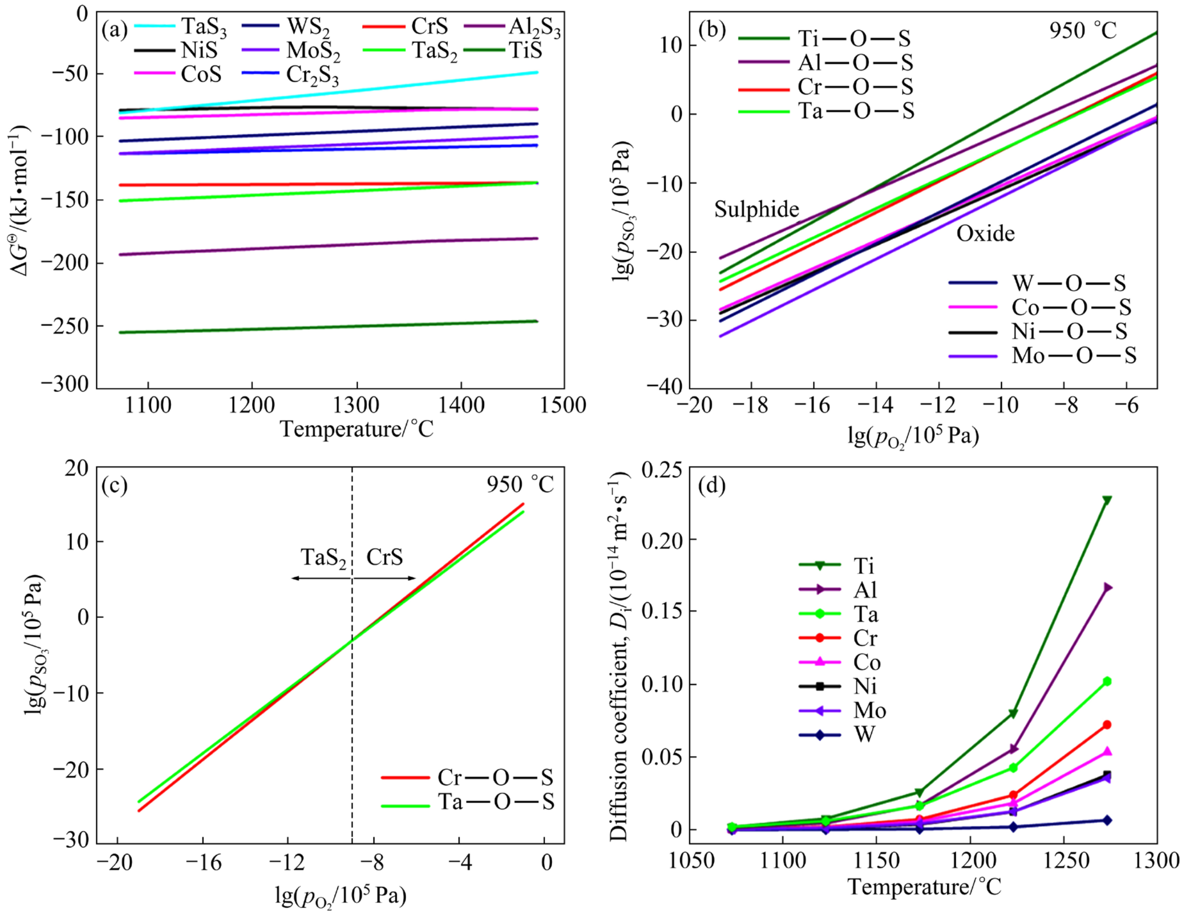

Fig. 13 (a) Ellingham diagram for sulphides of elements in DD98M alloy; (b, c) Superposition of thermodynamic phase stability diagrams; (d) Diffusion coefficient of elements in DD98M alloy at different temperatures

require low oxygen partial pressure, such as Cr and Ta (Fig. 10(c)). The formation of CrS is more likely to occur in places with higher oxygen/sulphur partial pressure, while the formation of TaS_2 is favored in places with lower oxygen/sulphur partial pressure (Fig. 13(c)). The distribution of TaS_2 and CrS is closely related to the oxygen partial pressure. At the initial stages illustrated in Fig. 10(b) and Fig. 12(d), the absence of the protective oxide film permits the rapid penetration of O and S into the matrix. At this stage, the alloy elements diffuse outward due to the content difference between the oxide layer and the matrix.

Figure 13(d) shows the diffusion coefficient of elements in the DD98M alloy (specific equations are given in Supporting Materials). Ti, Al and Ta elements preferentially diffuse to form a γ'-phase depleted layer, which produces a protective oxide layer beneath the non-protective oxide layer (Figs. 12(d, e)). At the same time, O and S further diffuse towards the substrate, while Cr diffuses within the γ'-phase depletion layer near the non-protective oxide film. The high oxygen partial pressure leads to the formation of Cr_2O_3 oxide, while low oxygen partial pressure and high S partial pressure induce the reaction of Cr to form CrS.

The cross-sectional morphologies of the DD98M alloy and the schematic diagrams of the sulfidation mechanisms are shown in Fig. 14. The formation of CrS further reduces the partial pressure of O and S. When O and S diffuse to the interface of the γ'-phase and the substrate, their low partial pressures make them favorable to interact with Ta, which has diffused to the interface, leading to the formation of TaS_2. Therefore, CrS and TaS_2 coexist in the alloy, and the S compound near the matrix is TaS_2, which is consistent with the SEM and TEM observations (Figs. 9, 10(c) and 14).

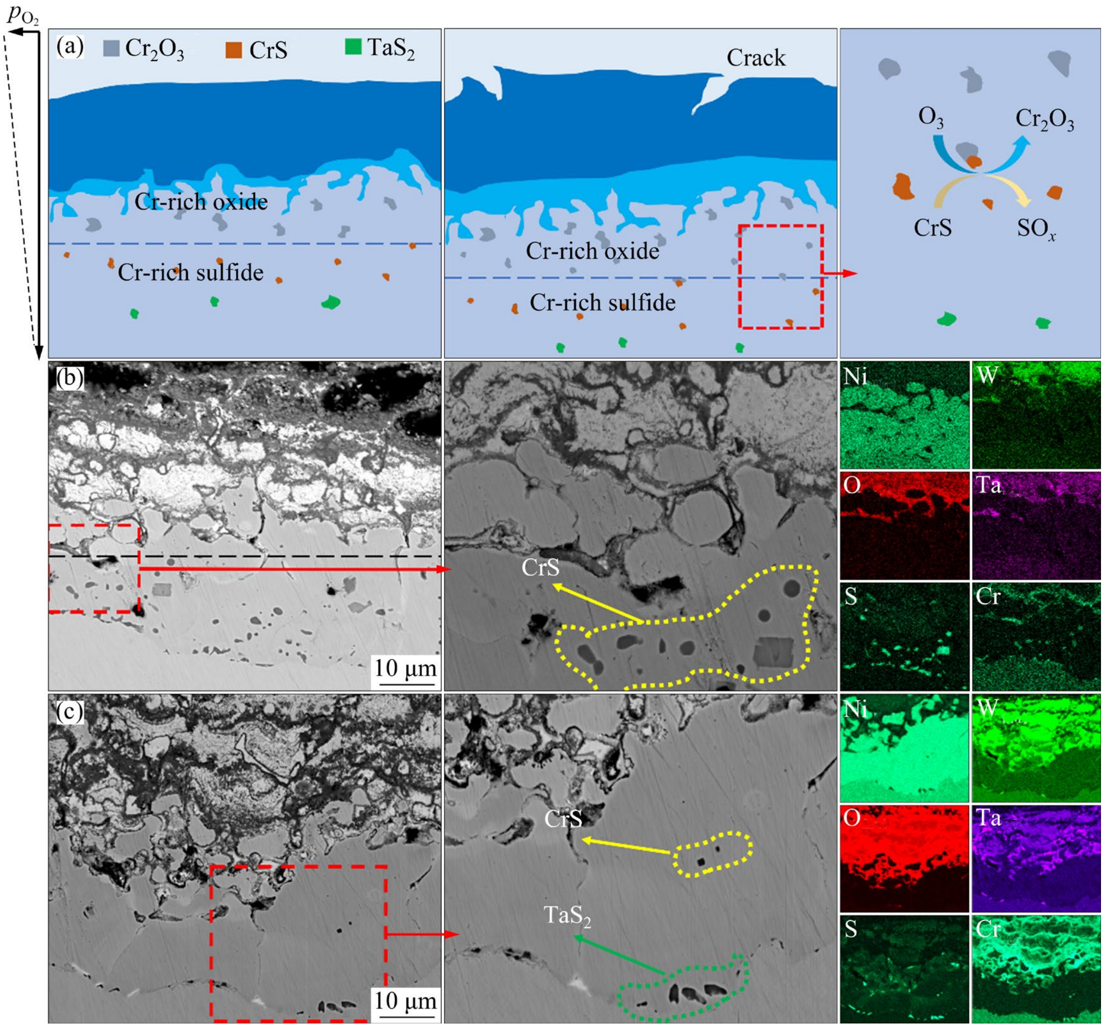

Fig. 14 Schematic diagrams of sulfidation mechanism of DD98M alloy (a), and cross-sectional morphologies of A2 (b) and A3 (c) alloys

4.2 Influence of impurity elements on hot corrosion behavior

The presence of microvoids is the primary cause for the shedding during hot corrosion. The microvoids are clearly observed in Fig. 6. The severer shedding of A3 alloy compared to the other two alloys may be attributed to the presence of these microvoids. The porosity is quantitatively determined through XRT, as shown in Figs. 15(a−c), in which the magnitude and location of the micropores are provided. The porosity is obtained by calculating the volume ratio of micropores to the test volume. The porosities of A1, A2 and A3 alloys are 0.088%, 0.133% and 0.187%, respectively. The variation in porosity should be attributed to the content of the impurity element N [26]. During the process of directional solidification, impurity elements tend to accumulate between dendrites, and N reacts to form N_2 when the dendrites solidify. The above reaction and the corresponding Gibbs free energy are described in Eqs. (11) and (12) [27]:

$$2[\mathrm{N}]_{\mathrm{melt}}=\mathrm{N}_2(\mathrm{g}) \tag{11}$$

$$\Delta G_{\mathrm{N}}=34518+37T+RT\ln\frac{p_{\mathrm{N}_2}}{a_{\mathrm{N}}^{2}} \tag{12}$$

The opening pressure p_{N_2} can be expressed by Eq. (13) when the reaction reaches equilibrium:

$$p_{\mathrm{N}_2}=\exp\left(\frac{-34518-37T}{RT}\right)\left(f_{\mathrm{N}}\cdot[\mathrm{N}]\right)^2 \tag{13}$$

The closed pore pressure is determined by the melt pressure (p_{melt}) and the surface tension (σ). The micropores are formed when Eq. (14) is satisfied, and the mechanism for micropore formation is shown in Fig. 15(d).

$$p_{\mathrm{N}_2}>p_{\mathrm{melt}}+{}^{2\sigma}\!/_{r} \tag{14}$$

where r is the radius of pore.

In general, there is an inverse relationship between the content of impurity elements (O, N, S) and surface tension. As impurity content increases, the surface tension decreases accordingly. The open-cell pressure of A1, A2 and A3 alloys is calculated by Eq. (13), whose value increases with the increase of N content, as shown in Fig. 15(e). The surface tension, on the other hand, is inversely proportional to the content of impurity elements. Therefore, the porosity of the alloys increases as the impurity content rises.

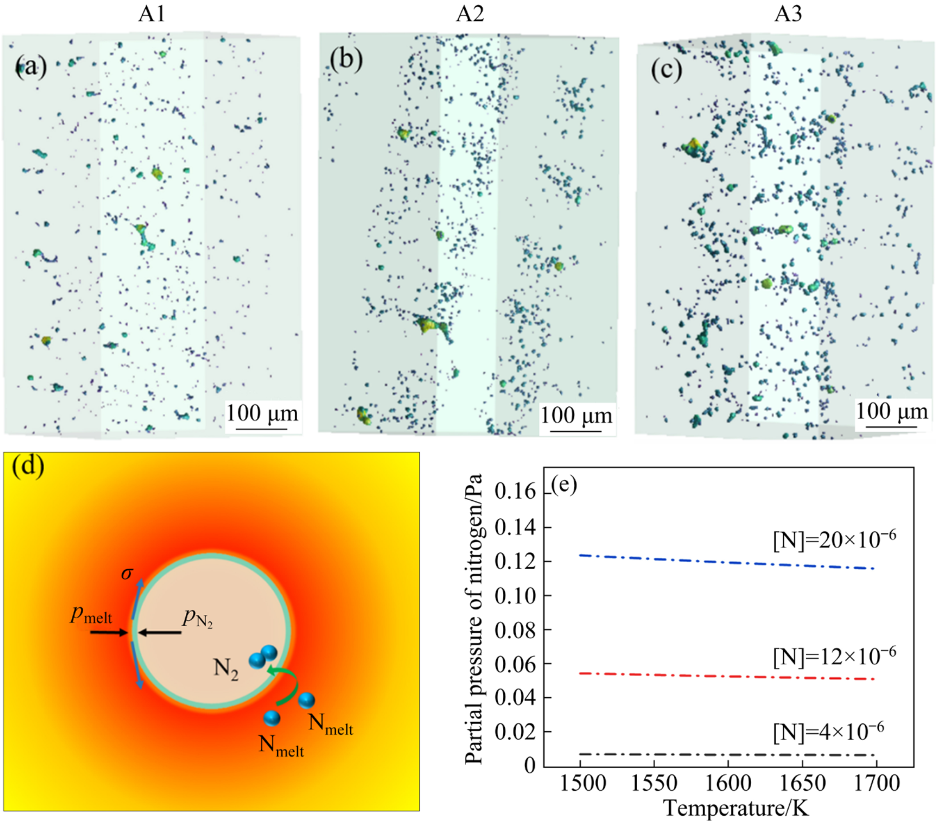

Fig. 15 Distribution and formation mechanism of micropores: (a−c) Distribution of micropores in A1, A2 and A3 alloys; (d) Schematic diagram for micropore formation; (e) Effect of N content on opening pressure of nitrogen at different temperatures

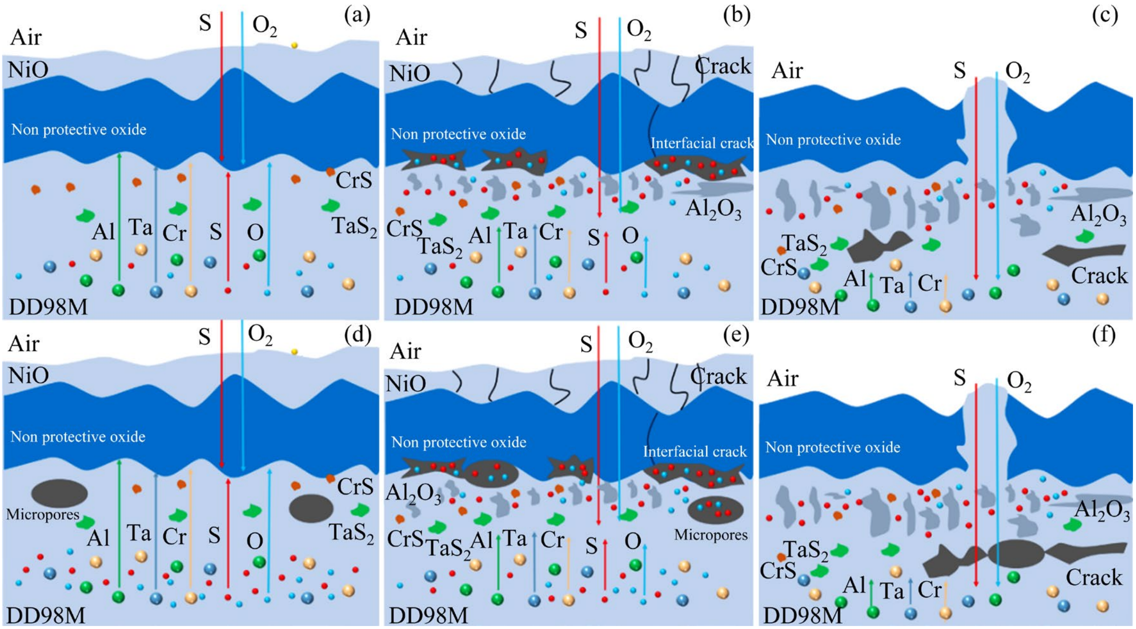

Fig. 16 Schematic diagram for corrosion mechanisms in DD98M alloy with different impurity contents: (a−c) A1 alloy; (d−f) A3 alloy

The corrosion mechanisms for the DD98M alloys with different impurity contents are illustrated in Fig. 16. During the initial stage of corrosion, a layer of NiO and an unprotective oxide film can be observed on the surface. The progression of hot corrosion involves not only the infiltration of S and O into the matrix, but also their outward diffusion, which creates a bidirectional diffusion pattern. The bidirectional diffusion accelerates the aggregation of O and S at the interface between the substrate and oxide film, promoting the formation of interfacial micropores. As corrosion progresses, micropores merge and develop into cracks (Fig. 16(b)). The cracks accelerate the diffusion of molten salts, resulting in the formation of more sulphides within the matrix and accelerating the corrosion of the alloy. Meanwhile, the diffusion of O and S is further accelerated, which gives rise to the oxidation of the sulphides and the alloy. The presence of cracks will also result in the rapid diffusion of chloride and a decrease in protective elements. At the same time, WO_3 produced by oxidation will also spread outward along the cracks and react with NiO at the edges of the cracks. The presence of W-rich oxides near the micropores in Fig. 6(b) supports this perspective.

The loss of elements will reduce the protective effect of the matrix and accelerate the corrosion reaction. However, the bidirectional diffusion and aggregation of higher content of impurity elements occur at a faster rate, resulting in the formation of more interfacial micropores. Consequently, the number of cracks induced by micropores will also increase (Fig. 16(e)). The formation of internal sulfide (in regions with low oxygen partial pressure) in the alloy with higher impurity content occurs more rapidly, and the rapid diffusion of O contributes to the internal sulfide-oxidation cycle. At the same time, there are more micropores in the alloy, which act as the rapid diffusion channels for O and S, thereby accelerating the sulfide-oxidation cycle of the alloy. Furthermore, the interconnection between the micropores and cracks promotes the formation of larger pores, which in turn lead to the detachment of the oxide film and result in severe corrosion.

5 Conclusions

(1) The DD98M alloys with different impurity contents show similar hot corrosion processes. Alloys with low impurity content exhibit better surface quality and thinner corrosion layer compared to those with high impurity content, which shows better hot corrosion resistance.

(2) During hot corrosion, the mixed salt of Na_2SO_4 and NaCl exhibits a synergistic effect on corrosion. The Na_2SO_4 induces basic corrosion, while NaCl accelerates the corrosion reaction.

(3) An increase of the N content in the alloy

results in an increase of porosity. These micropores act as channels for the rapid infiltration of both salt mixture and oxygen, thereby accelerating corrosion. Furthermore, the bidirectional diffusion of O and S not only intensifies the formation of interface cracks, but also contributes to the overall corrosion process.

CRediT authorship contribution statement

Geng-yi DONG: Conceptualization, Formal analysis, Writing − Original draft, Writing − Original draft preparation, Methodology, Data curation; **Yijiala YILITI:** Conceptualization, Formal analysis, Writing − Original draft, Writing − Original draft preparation; **Run-ze YU:** Data analysis, Writing − Review and editing; **Jie MENG:** Data analysis, Writing − Review and editing; **Wen-jun HAN:** Data analysis, Writing − Review and editing; **Kai CHANG:** Data analysis, Writing − Review and editing; **Qi-fei ZHANG:** Data analysis; **Xiao-gang YOU:** Conceptualization, Formal analysis, Writing − Original draft, Methodology, Data curation, Funding acquisition, Project administration and supervision; **Yi-nong WANG:** Writing − Original draft preparation, Project administration and supervision.

Declaration of competing interest

The authors declare that they have no known competing financial interests or personal relationships that could have appeared to influence the work reported in this paper.

Acknowledgments

The authors gratefully acknowledge financial support from the National Key Research and Development Project of China (No. 2019YFA0705300), the National Natural Science Foundation of China (No. 52004051), the Project of Zhongyuan Critical Metals Laboratory, China (No. GJJSGFYQ202321), and the Fund for Priority Support of Research Projects by Returned Overseas Scholars in Henan Province, China.

Supporting Materials

Supporting Materials in this paper can be found at: https://tnmsc.csu.edu.cn/download/12-p0522-2024-0629-Supporting_Materials.pdf.

References

[1] GUDIVADA G, PANDEY A K. Recent developments in nickel-based superalloys for gas turbine applications: Review [J]. Journal of Alloys and Compounds, 2023, 963: 171128.

[2] AI Cheng, LI Kai-wen, GUO Min, HUANG Tai-wen, LIU Lin. Research progress of low cost second-generation Ni-based single crystal superalloys [J]. The Chinese Journal of Nonferrous Metals, 2024, 34(9): 2857−2868. (in Chinese)

[3] ZHOU Peng-jie, YU Jin-jiang, SUN Xiao-feng, GUAN Heng-rong, HU Zhuang-qi. Roles of Zr and Y in cast microstructure of M951 nickel-based superalloy [J]. Transactions of Nonferrous Metals Society of China, 2012, 22: 1594−1598.

[4] WANG Kai-ming, LIU Wei, DU Dong, CHANG Bao-hua, LIU Guan, HU Yong-le, TONG Yong-gang, ZHANG Ming-jun, ZHANG Jian, JU Jiang. Microstructure and properties of K648 superalloy additively manufactured by extreme high-speed laser metal deposition [J]. Transactions of Nonferrous Metals Society of China, 2024, 34: 2192−2203.

[5] SONG Peng, LIU Ming-feng, JIANG Xiang-wei, FENG Yu-chao, WU Jun-jie, ZHANG Gong, WANG Dong, DONG Jia-sheng, CHEN Xing-qiu, LOU Lang-hong. Influence of alloying elements on hot corrosion resistance of nickel-based single crystal superalloys coated with Na_2SO_4 salt at 900 °C [J]. Materials & Design, 2021, 197: 109197.

[6] MENG Jun-sheng, CHEN Ming-xuan, SHI Xiao-ping, MA Qiang. Effect of Co on oxidation and hot corrosion behavior of two nickel-based superalloys under Na_2SO_4−NaCl at 900 °C [J]. Transactions of Nonferrous Metals Society of China, 2021, 31: 2402−2414.

[7] YANG Rui-ning, HAN San-xuan, LEI Xiao-wei, LIU Jing-bo, MA Jin-cen, ZHANG Jie, WANG Nan. Hot corrosion mechanism of laser metal deposited Ni-based single crystal superalloy under fuel gas atmosphere [J]. Surface and Coatings Technology, 2023, 474: 130057.

[8] MONTERO X, ISHIDA A, MEIβNER T M, MURAKAMI H, GALETZ M C. Effect of surface treatment and crystal orientation on hot corrosion of a Ni-based single-crystal superalloy [J]. Corrosion Science, 2020, 166: 108472.

[9] DAROLIA R. Development of strong, oxidation and corrosion resistant nickel-based superalloys: Critical review of challenges, progress and prospects [J]. International Materials Reviews, 2019, 64: 355−380.

[10] SYED A U, MARTINEZ F D, ROBERTS T, ENCINAS-ORROPESA A, MORAR N I, GROHNE M, FROMMHERZ M, NICHOLLS J R, GRAY S. Performance comparison between isothermal hot corrosion and in situ cyclic hot corrosion of nickel-based superalloys [J]. Oxidation of Metals, 2021, 96: 43−55.

[11] RAPP R A. Chemistry and electrochemistry of hot corrosion of metals [J]. Materials Science and Engineering, 1987, 87: 319−327.

[12] OTSUKA N, RAPP R A. Effects of chromate and vanadate anions on the hot corrosion of preoxidized Ni by a thin fused Na_2SO_4 film at 900 °C [J]. Journal of the Electrochemical Society, 1990, 137: 53−60.

[13] CHANG J X, WANG D, ZHANG G, LOU L H, ZHANG J. Interaction of Ta and Cr on Type-I hot corrosion resistance of single crystal Ni-base superalloys [J]. Corrosion Science, 2017, 117: 35−42.

[14] LI Jin-guo, SUN Jing-xia, LIU Jin-lai, SUN Xiao-feng. The precipitation and effect of topologically close-packed phases

in Ni-based single crystal superalloys [J]. Journal of Materials Science & Technology, 2024, 173: 149−169.

[15] SHI Liang-quan, ZHANG Yun-shu, SHI Sheng-tai. The low temperature hot corrosion of iron and iron-aluminum alloys [J]. Corrosion Science, 1992, 33: 1427−1438.

[16] HU Shan-shan, FINKLEA H, LIU Xing-bo, A review on molten sulfate salts induced hot corrosion [J]. Journal of Materials Science & Technology, 2021, 90: 243−254.

[17] ZHAO Bin, WANG Qi-lin, REN Yan-jie, HAN Lin-hu, JIANG Dong-fang. Hot corrosion behavior of Inconel 625 alloys fabricated by selective laser melting [J]. The Chinese Journal of Nonferrous Metals, 2024, 34(6): 2030−2042. Chinese. (in Chinese)

[18] PETTIT F S, MEIER G H, GELL M, KARTOVICH C S, RADOVICH J F. Oxidation and hot corrosion of superalloys [C]//Superalloys. Warrendale, USA: Metallurgical Society of AIME, 1984: 651−687.

[19] YANG Fang-min, LIAN Li-xian, LIU Ying, GONG Xiu-fang. Mechanism of adding rhenium to improve hot corrosion resistance of nickel-based single-crystal superalloys [J]. Rare Metals, 2021, 40: 2076−2082.

[20] CHANG J X, WANG D, LIU X G, LOU L H, ZHANG J. Effect of rhenium addition on hot corrosion resistance of Ni-based single crystal superalloys [J]. Metallurgical and Materials Transactions A, 2018, 49: 4343−4352.

[21] ZHAN Xin, WANG Dong, ZHANG Zong-peng, ZHANG Jian. Effect of trace sulfur on the hot corrosion resistance of Ni-base single crystal superalloy [J]. Corrosion Science, 2023, 224: 111528.

[22] LI Yi, TAN Yi, YOU Xiao-gang, WANG Ding-gang, HU Ye-bing, SONG Shuang, QIANG Jian-bing. Effect of trace impurity elements on the high-temperature oxidation resistance of a high-purity nickel-based superalloy [J]. Corrosion Science, 2023, 211: 110904.

[23] ZHANG Ang, GUO Zhi-peng, JIANG Bin, DU Jing-lian, WANG Cui-hong, HUANG Guang-sheng, ZHANG Ding-fei, LIU Feng, XIONG Shou-mei, PAN Fu-sheng. Multiphase and multiphysics modeling of dendrite growth and gas porosity evolution during solidification [J]. Acta Materialia, 2021, 214: 117005.

[24] RAPP R A, OTSUKA N. The role of chromium in the hot corrosion of metals [J]. ECS Transactions, 2009, 16: 271−282.

[25] TAO Xi-peng, WANG Xin-guang, MENG Jie, ZHOU Yi-zhou, LI Jin-guo, SUN Xiao-feng. Abnormal improvement of high-temperature stress rupture life in a new low cost Ni-based single crystal superalloy by adding minor nitrogen [J]. Materials Science and Engineering: A, 2023, 872: 144980.

[26] WADA H, GUNJI K, WADA T. Solubility of nitrogen in molten Fe−Ni and Fe−Cr alloys [J]. Transactions of the Iron and Steel Institute of Japan, 1968, 32: 933−938.

[27] YOU Xiao-gang, DONG Geng-yi, ZHOU Hai-jing, ZHANG Hui-xing, TAN Yi, WANG Yi-nong, LI Peng-ting, YOU Qi-fan, LI Yi, CUI Hong-yang, LIU Yu-feng, YUAN Hua. Removal of oxygen, nitrogen, and inclusions in powder superalloy scraps by electron beam smelting and induced solidification and the purification mechanisms [J]. Separation and Purification Technology, 2023, 304: 122290.

微量杂质元素对 DD98M 合金耐高温腐蚀性能的影响

董庚益[1]，伊加拉·伊力提[2]，于润泽[2]，孟　杰[3]，韩文君[2]，常　凯[2]，张琦飞[1]，游小刚[1]，王轶农[2]

1. 郑州大学 中原关键金属实验室，郑州 450001；
2. 大连理工大学 材料科学与工程学院，大连 116024；
3. 中国科学院 金属研究所 师昌绪先进材料创新中心，沈阳 110016

摘　要：研究了不同含量杂质元素对 DD98M 合金在 950 ℃下 Na_2SO_4+NaCl 混合盐中耐热腐蚀性能的影响。结果表明，随着杂质含量的增加，DD98M 合金的耐腐蚀性能显著下降。氮的存在导致合金孔隙率增加。这些微孔促进熔盐和氧气向合金内部快速扩散，加速氧和硫的双向扩散，从而导致这些元素在氧化物−基体界面上积累。这一过程促进了界面裂纹的萌生和扩展。建立了一个含不同杂质元素合金热腐蚀产物的生长模型。

关键词：熔盐；DD98M 合金；热腐蚀；杂质元素

(Edited by Xiang-qun LI)